Carbon and vacancy centers in hexagonal boron nitride

P. Huang [1,2,3] M. Grzeszczyk [1,2] K. Vaklinova [1,2] K. Watanabe [4] T. Taniguchi [5]
K. S. Novoselov [1,2] and M. Koperski [1,2,*]

[1] *Department of Materials Science and Engineering, National University of Singapore, 117575, Singapore*
[2] *Institute for Functional Intelligent Materials, National University of Singapore, 117544, Singapore*
[3] *Guangxi Key Laboratory of Information Materials, Guilin University of Electronic Technology, Guilin 541004, China*
[4] *Research Center for Functional Materials, National Institute for Materials Science, Tsukuba, Ibaraki 305-0044, Japan*
[5] *International Center for Materials Nanoarchitectonics, National Institute for Materials Science, Ibaraki 305-0044, Japan*

(Received 29 December 2021; revised 25 May 2022; accepted 5 July 2022; published 21 July 2022)

The creation of defect with predetermined optical, chemical, and other characteristics is a powerful tool to enhance the functionalities of materials. Herewith, we utilize density functional theory to understand the microscopic mechanisms of formation of defects in hexagonal boron nitride based on vacancies and substitutional atoms. Through in-depth analysis of the defect-induced band structure and formation energy in varying growth conditions, we uncovered a dominant role of interdefect electron pairing in stabilization of defect complexes. The electron reorganization modifies the exchange component of the electronic interactions which dominates over direct Coulomb repulsion or structural relaxation effects making the combination of acceptor- and donor-type defect centers energetically favorable. Based on an analysis of a large number of defect complexes we develop a simple picture of the inheritance of the electronic properties when individual defects are combined together to form more complex centers.

DOI: 10.1103/PhysRevB.106.014107

I. INTRODUCTION

Controllable formation of defect in crystals is a pathway towards observation of novel phenomena, tailoring material properties and enabling new functionalities [1]. Successful formation of specific defects typically requires knowledge about microscopic mechanisms of defect-lattice or interdefect interactions. Defect stability needs to be understood in relation to the electronic properties of the defect-enriched material [2–10]. With the recent observation of single photon emitters in hexagonal boron nitride (hBN), the intentional creation of defect centers became a technologically important challenge. hBN is a representative of two-dimensional insulators [11,12] hosting a variety of defect centers that activate midgap photoluminescence (PL) in ultraviolet, visible, and near-infrared spectral regions [13–19]. These luminescent centers appear spontaneously in different types of hBN crystals: mechanically exfoliated layers, micro- and nanoscale powders, chemical vapor deposition or metal-organic vapor deposition grown thin films [20]. They can also be created and/or enhanced via annealing, irradiation, or straining of hBN layers. Some of these defects are currently associated with carbon impurities, which can be introduced *in situ* during crystal growth or via postgrowth annealing of pristine hBN crystals in carbon-rich atmosphere [21,22].

The optical response of the carbon-doped hBN is likely dominated by the carbon impurities and/or vacancies that can be found in pristine hBN films. The combination of single-site vacancies and carbon substitutions creates a vast parameters space to be explored when considering defect-related optical transitions. The complexity of the problem is reflected in the PL response of carbon-doped hBN films [21–28]. The defect-induced optical processes are manifested in the form of multiresonance patterns with well-defined energy of transitions [Fig. 1(a)] or appear as more disordered systems characterized by broad-band emission attributed to ensembles of defects [Fig. 1(b)].

In order to understand the probability of defect formation in various experimental conditions, we investigated systematically the electronic properties and stability of carbon and vacancy centers in hexagonal boron nitride. We can classify these centers by their complexity ranging from single-site substitutions and vacancies to clusters of defects as illustrated schematically in Fig. 2 [29]. Through a comparative analysis of the defect properties, we have found that it is energetically favorable to couple two elementary defects together through a mechanism of interdefect electron pairing. The process of combining defects resembles the formation of interatomic chemical bonds, determined by the competition between the Coulomb and exchange interactions arising from overlapping atomic orbitals [30,31]. We demonstrate that within a hBN lattice the combination of carbon and/or vacancy centers introduces elegant symmetries within the electronic band structure, leading to robust stabilization of the defect complexes. The mechanism is driven by the modification of the exchange terms, which dominate over the increased Coulomb repulsion.

II. SINGLE- AND DOUBLE-SITE DEFECT CENTERS

Pristine hBN lattice is composed of van der Waals bonded monolayers in an AA′ stacking configuration. A monolayer

*msemaci@nus.edu.sg

 ©2022 American Physical Society

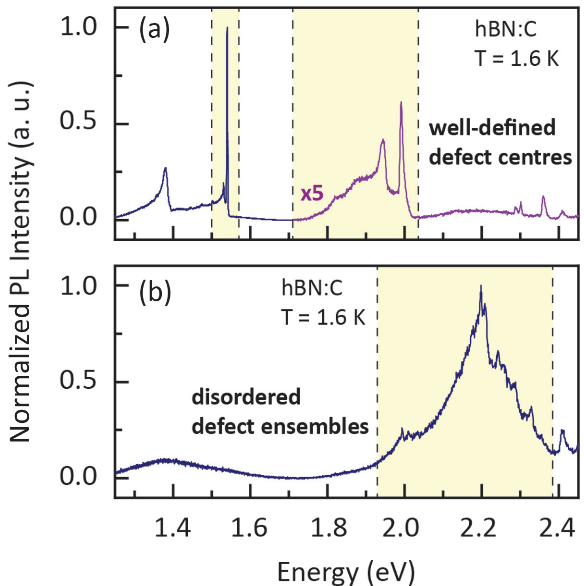

FIG. 1. Example low temperature (1.6 K) μPL spectra of carbon-doped hBN films characterized by few tens of nanometer thickness. (a) A reproducible pattern of optical resonances with well-defined energy of transitions is the most common optical response. (b) Some crystals are characterized by emission spectra that are dominated by broader PL bands composed of a series of narrow lines indicative of a more disordered defect ensemble.

hBN is characterized by a hexagonal structure with two triangular sublattices occupied by boron and nitrogen. The existence of two different atoms in the elementary cell breaks the symmetry of the hexagonal lattice, which leads to an opening of the band gap of about 6.0 eV in the bulk limit. The in-plane interatomic σ-type bonding between boron and nitrogen arises from sp^2 hybridization. It is predominantly responsible for the structural stability of the crystal. The fundamental valence and conduction bands are constructed from π bonded and π^* antibonded orbitals, respectively.

Carbon doping of hBN leads to the creation of elemental impurities such as carbon substitution for boron (C_B) or carbon substitution for nitrogen (C_N). Both defect centers give rise to a spin-split midgap level. The defect-induced level is located below the conduction band for C_B creating a donor state or above the valence band for C_N creating an acceptor state as illustrated in Figs. 3(a) and 3(b). These donor and acceptor states are constructed from half-filled p_z orbitals of carbon atoms as shown in Figs. 3(d) and 3(e). The corresponding wave function exhibits an oscillatory character, whose amplitude decays over the next few atoms in the vicinity of the impurity. Combining C_N and C_B defects together to form a C_NC_B dimer impacts qualitatively the electronic structure of the defect. C_NC_B can be considered as a simple molecule embedded within a hBN lattice with energy levels defined by π bonding between p_z orbitals of the C atoms at N and B sites. As a result of the C-C bonding the spin splitting is lifted via reorganization of the electrons from occupying C_N and C_B states to occupying a molecularlike C_BC_N level. Consequently, the electronic structure of C_BC_N defect resembles the highest occupied molecular orbital (HOMO) and lowest unoccupied molecular orbital (LUMO) levels residing above the valence-band edge and below the conduction-band edge, respectively. The HOMO level is fully occupied and the LUMO level is empty, leading to the removal of the spin splitting observable for single-site C defects and spatial extension of the wave function as seen in Fig. 3(f).

Interestingly, the electronic configuration of B, C, and N in combination with the electronic band structure of hBN leads to unique stabilization mechanisms for carbon and vacancy centers. We investigate the formation energy of single-site defects and their double-site combinations by density functional theory (DFT) for nitrogen- and boron-rich conditions (see the Methods section for the detailed computational procedure). We define the stabilization energy of multisite defects as the differential formation energy between the defect complex and the sum of the constituent single-site defects:

$$E_{\text{stab}}(D) = E_f(D) - \sum_i E_f(D_i),$$

where $E_{\text{stab}}(D)$ is the stabilization energy for defect D, $E_f(D)$ is the formation energy for defect D, and $E_f(D_i)$ is the formation energy of single-site constituent defects D_i which combine to form defect D. We found that the stabilization energy is negative for all investigated vacancy- and carbon-based defect complexes as illustrated in Figs. 4(a) and 4(b) in agreement with previous calculations [7,32]. This observation indicates that it is energetically favorable to combine simple defects within the hBN lattice to form more complex lattice imperfections. In carbon-doped hBN the dominant mechanism of the reduction of formation energy originates from the reorganization of the electronic structure related to the bond formation. When combining C_N and C_B defects to form the C_BC_N dimer, the electron occupying the C_B donor state relaxes onto the hybridized C_BC_N state. That process dominates over the Coulomb repulsion originating from placing two electrons on the same molecular level and over the energy modification due to defect-induced structural relaxation. Such robust stabilization mechanism via electronic reconfiguration occurs due to the large energy separation of the donor and acceptor states enabled by the hBN band gap. A schematic illustration of the generalized mechanism is presented in Fig. 4(c).

The origin of the stabilization mechanism stems from the quantum-mechanical description of the defect states. When two elementary defects are spatially separated from each other, the correlation between the electrons residing at defect levels is negligible. For example, isolated C_B and C_N impurities can be described by the single-particle wave function ϕ_B and ϕ_N [see Figs. 3(d) and 3(e)] that fulfill the Schrödinger equations:

$$\left(T_1 - V_N^1\right)\phi_N = E_1\phi_N,$$
$$\left(T_2 - V_B^2\right)\phi_B = E_2\phi_B,$$

where T_1, T_2 is the kinetic energy of the electron at the defect level and V_N^1 and V_B^2 represent the Coulomb potential energy of

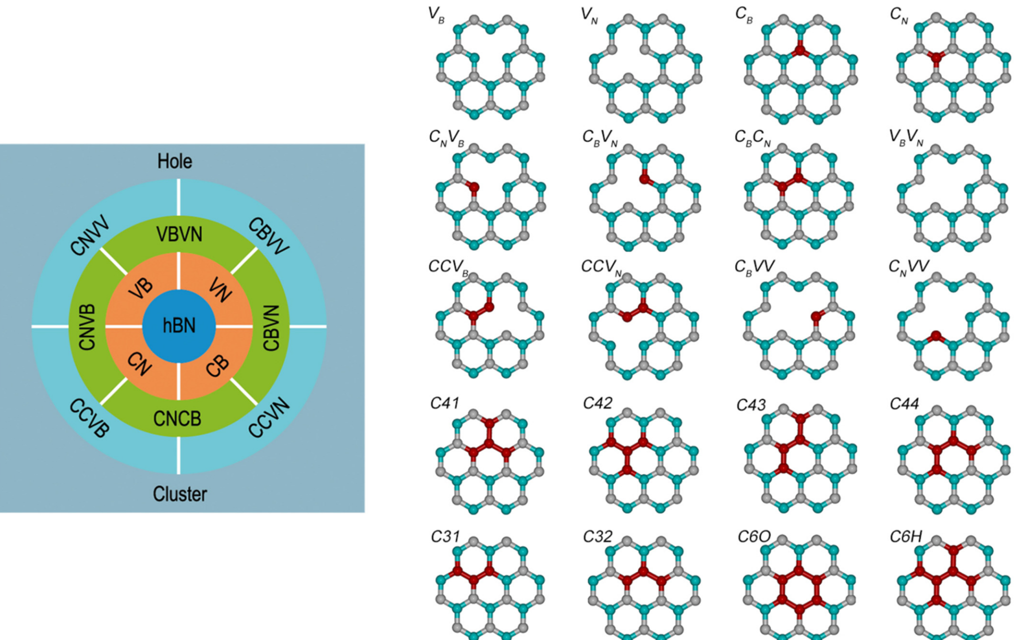

FIG. 2. The atomic structure of the vacancy and carbon defect centers considered in current work. Such defect library is characterized by a hierarchical structure, when more complex lattice imperfections can be formed from simpler constituent defects. Merging of the defects may be investigated from the point of view of the lattice stability or inheritance of the electronic properties. The left diagram shows this hierarchy of defects in hBN from single substitution and vacancy to impurity and/or cluster. The atomic structures of selected single-site, double-site, and triple-site defects and more complex clusters are listed. The defect notations C_BC_N and V_BV_N for triple defects are replaced by CC and *VV* in short. The C6O and C6H represent the carbon clusters in the ring and "H" shape, respectively.

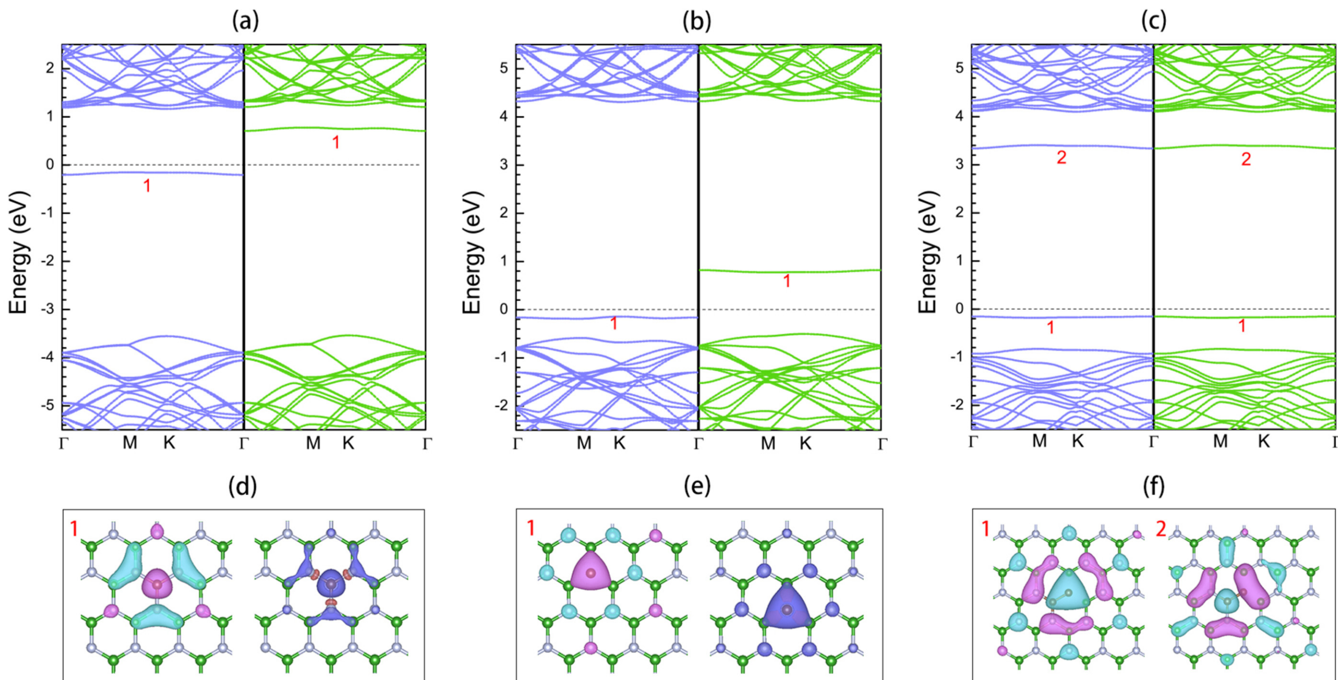

FIG. 3. Spin-projected band structure of hBN in the presence of carbon substitution centers: (a) C_B, (b) C_N, and (c) C_BC_N. (d)–(f) The top view of Γ-point wave functions (real part) illustrates the defect states marked by numbers (1 or 2) in the corresponding band diagrams. The colorcoding (pink, light blue) represents opposite signs of the wave function. (d),(e) The total spin density is presented with color coding (purple, brown) depicting spin up and down states.

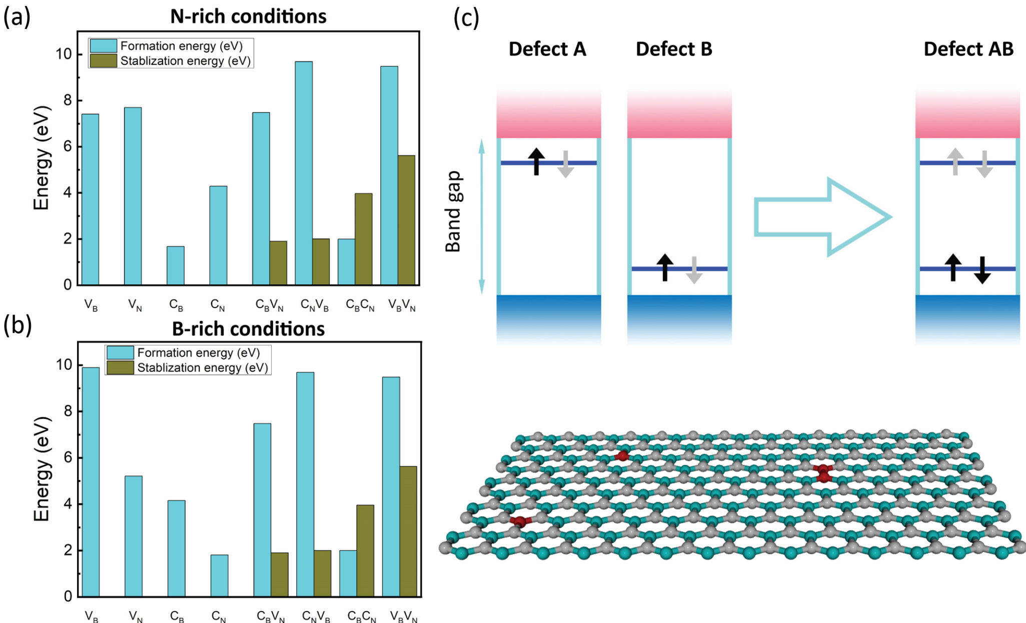

FIG. 4. The histograms represent formation energy for single-site and double-site defect centers in (a) nitrogen-rich and (b) boron-rich conditions together with the absolute value of the stabilization energy for double-site defects. (c) A schematic diagram illustrates a process of combining two defects that give rise to half-occupied donor and acceptor states. The combination results in a defect that displays molecularlike occupied and empty levels. The mechanism provides a significant contribution to the large values of the stabilization energy observed for more complex vacancy and carbon defect centers in hBN.

the carbon impurity electrons at the N and B sites contributed by the atomic nuclei and band electrons.

When the two substitutions are combined to occupy the neighboring lattice sites, the Hamiltonian of the system needs to be modified to account for interdefect interactions:

$$H = (T_1 + T_2) - V_B^1 - V_N^1 - V_B^2 - V_N^2 + \frac{e^2}{4\pi\varepsilon\varepsilon_0 r_{12}} + \frac{e^2}{4\pi\varepsilon\varepsilon_0 R_{NB}}.$$

Apart from additive single-defect terms, the Hamiltonian includes the Coulomb potential originating from the neighboring defect sites (represented by V_N^2 and V_B^1) as well as electron-electron and core-core electrostatic interactions in the screening environment of band electrons (described by the dielectric constant ε).

The many-body state arising from such Hamiltonian, which describes the spatial component of the wave function, takes the form

$$\Phi(r_1, r_2) = \frac{1}{\sqrt{2(1 \pm S^2)}}[\phi_N(r_1)\phi_B(r_2) \pm \phi_N(r_2)\phi_B(r_1)],$$

where $S = \langle\phi_B|\phi_N\rangle$ is the overlap integral. The positive and negative signs correspond to the bonding and antibonding states, respectively. The many-body state is enriched with an additional term arising due to the exchange of electrons between the N and B substitution sites. The energy of the bonded (E_+) and antibonded (E_-) state can be therefore expressed as

$$E_\pm = \langle\Phi(r_1, r_2)|H|\Phi(r_1, r_2)\rangle = E_0 + \frac{K \pm J}{\sqrt{1 \pm S^2}},$$

where E_0 is the sum of single-defect energies, K is the Coulomb energy given by

$$K = \langle\phi_N(r_1)\phi_B(r_2)| - V_B^1 - V_N^2 + \frac{e^2}{4\pi\varepsilon\varepsilon_0 r_{12}} + \frac{e^2}{4\pi\varepsilon\varepsilon_0 R_{NB}}|\phi_N(r_1)\phi_B(r_2)\rangle.$$

The Coulomb energy takes into account the electron-core attraction, electron-electron repulsion, and core-core repulsion. Such electrostatic interaction is usually dominated by the repulsive forces; however, the exact contribution of each term depends on the type of defect center. For the C_NC_B defect complex, the on-site electron-electron repulsion provides the strongest contribution and constitutes the dominating term for the Coulomb energy.

The J parameter is the exchange integral:

$$J = \langle\phi_N(r_2)\phi_B(r_1)| - V_B^1 - V_N^2 + \frac{e^2}{4\pi\varepsilon\varepsilon_0 r_{12}} + \frac{e^2}{4\pi\varepsilon\varepsilon_0 R_{NB}}|\phi_N(r_2)\phi_B(r_1)\rangle.$$

The increased Coulomb repulsion in the bonded state for the C_NC_B dimer is compensated by the modification of exchange integral leading to the large value of the stabilization energy as described above.

The electron pairing mechanism has a direct impact on the optical response of the defect-enriched hBN through the contribution of the defect states to the dielectric function as illustrated in Fig. 5. For C_B and C_N defects, the low-energy optical response (1–3 eV) is dominated by the transitions

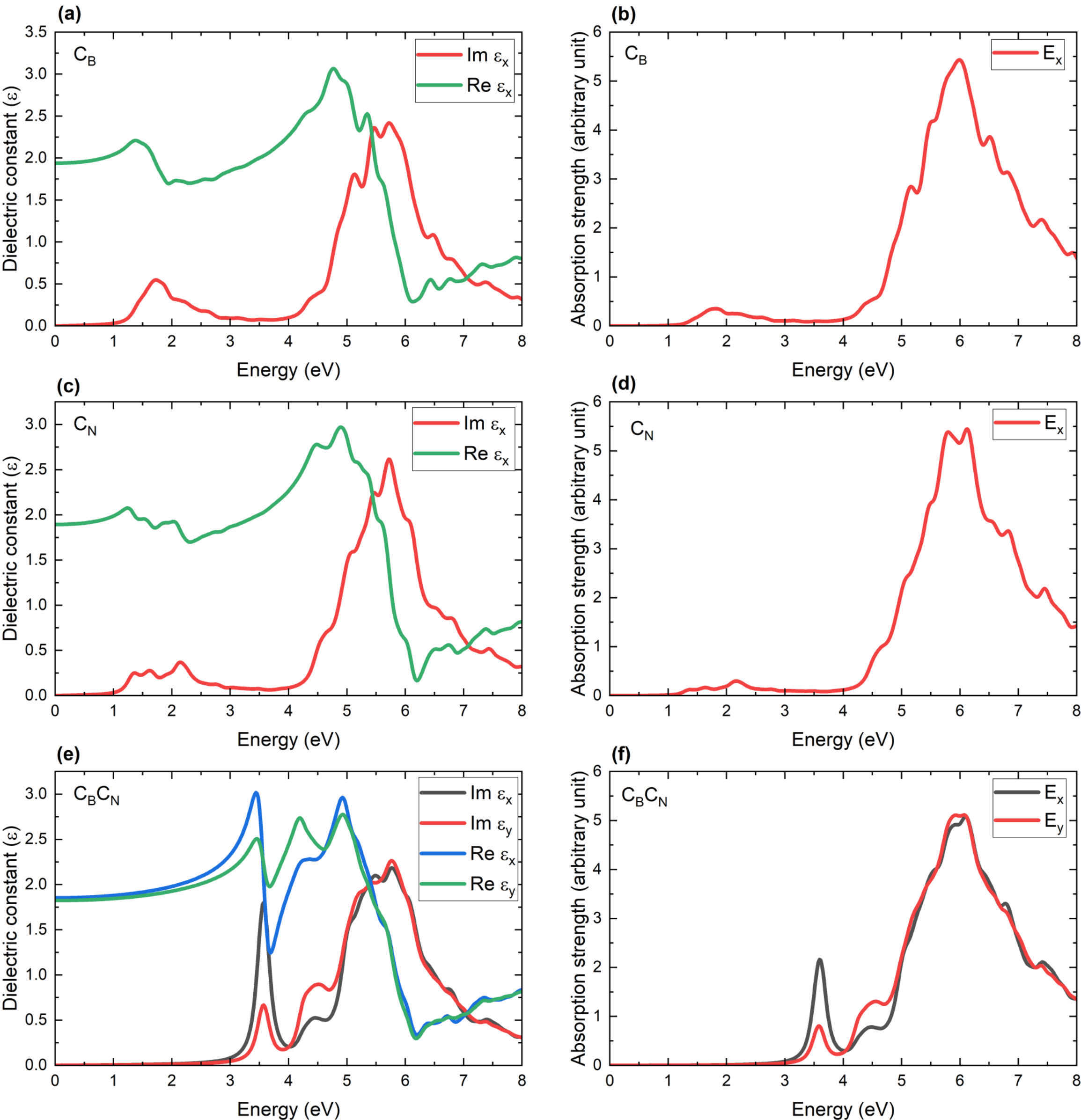

FIG. 5. The DFT calculated dielectric constant $\varepsilon = (\varepsilon_x, \varepsilon_y)$ and absorption strength of the (a),(b) C_B, (c),(d) C_N, and (e),(f) C_BC_N defects. Due to the D_{3h} symmetry of the C_B and C_N defects, ε_x and ε_y components of the dielectric constant are identical, therefore only the ε_x component is demonstrated. For the C_BC_N defect, the symmetry is reduced resulting in distinction between the ε_x and ε_y compnents. The absorption strength is calculated from the dielectric constant coefficient as escribed in the Methods section.

between the defect level and the electronic bands of the host lattice. For C_B, these are the transitions between the occupied defect level and the conduction subbands. For C_N, these are the transitions from the valence subbands to the empty defect level. These contributions have a broad-band character inherited from the dispersive electronic bands of the hBN crystal. The defect-band transitions become inactive in C_NC_B defect due to the electron pairing mechanism, as the molecularlike state (LUMO) below the conduction band becomes empty and the molecularlike state (HOMO) above the valence band becomes fully occupied. Such electronic reorganization leads to the appearance of a resonant HOMO-LUMO transition at higher energy (about 3.6 eV). Further modification of the optical spectra can be expected through incorporation of many-body effects, such as formation of defect-bound exciton states [33] or local modification of the lattice through external stimuli [34].

A qualitatively similar pairing mechanism is also applicable to the combination of two vacancies in hBN. The formation energy for a nitrogen (V_N) or boron (V_B) vacancy is larger than for carbon substitutions at corresponding lattice sites (C_N or C_B) as they require breaking of three strong sp^2 bonds. The V_N defect gives rise to midgap states akin to C_B. Half-filled level emerges below the conduction band with an addition of two more empty defect levels located within the conduction band as seen in Fig. 6(a). The V_B defect creates three half-filled levels. The occupied states are buried within the valence band, while the empty states emerge above the valence band as illustrated in Fig. 6(b). These states originate from the dangling bonds of the B atom for the V_N defect

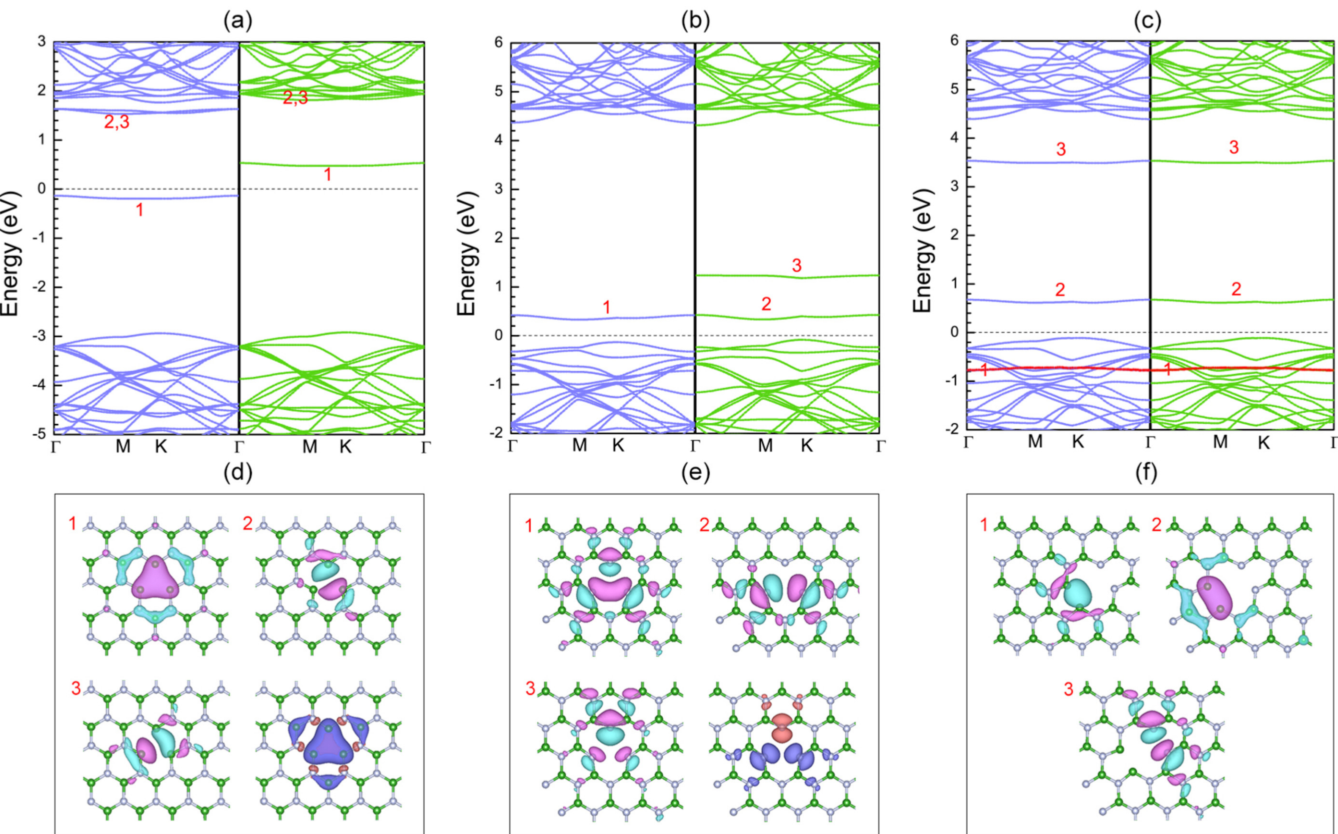

FIG. 6. Spin-projected band structure of hBN in the presence of vacancy centers: (a) V_N, (b) V_B, and (c) V_BV_N. The red line in (c) highlights the defect state of V_BV_N located within the valence band. (d)–(f) The top view of Γ-point wave functions (real part) illustrate the defect states marked by numbers (1, 2, or 3) in the corresponding band diagrams. The color coding (pink, light blue) represents opposite signs of the wave function. (d),(e) The total spin density is presented with color coding (purple, brown) depicting spin up and down states.

and from the dangling bonds of the N atom for the V_B defect. The orbital wave functions for these states exhibit more delocalized character when compared to carbon substitutions as visualized in Figs. 6(d)–6(f). Consequently, the stabilization energy for the V_BV_N defect is larger than for the C_BC_N defect. The V_BV_N defect creates three molecularlike levels; however, the occupied state is located within the valence band, so that the relaxation of the electron from V_N states leads to the increase of the stabilization energy. Additionally, the combination of two vacancies together reduces the number of the broken bonds from six to four. Overall, in the combined V_BV_N state, the three defect-induced levels are of the following origin: (1) the empty state below the conduction band arises due to the in-plane σ^* bond of the N-N pair, (2) the empty states above the valence band arise due to the out-of-plane π-bonded p_z orbitals of the B-B pair, and (3) the occupied state located within the valence band arises due to the in-plane bond of the B-B pair.

III. TRIPLE-SITE DEFECTS AND CARBON CLUSTERS

The trend of observing negative stabilization energy persists for triple-site defects as demonstrated in Fig. 7. The triple-site defect in carbon-doped hBN may be formed by combining the carbon dimer with a vacancy, a vacancy dimer with a single carbon substitution, or by creating vacancy or carbon trimers. Here, we will focus on inheritance effects when a carbon dimer is merged with a vacancy. As demonstrated in Fig. 8, the $C_BC_NV_B$ defect gives rise to four midgap states of different origin. The fully occupied state above the valence band emerges from π bonding of the C-C dimer and can be considered as an inherited HOMO state. The half-filled state above the valence band originates from the dangling bond of the N atom created by the vacancy. Additionally, two empty states below the conduction band arise due to in-plane σ^* C-B antibonding enabled by the presence of the vacancy (lower energy state) and π^* out-of-plane C-C bonding (higher energy state). Generally speaking, $C_BC_NV_B$ creates states that are inherited from the C-C dimer and from the vacancy as well as qualitatively new states due to the presence of a vacancy next to a carbon substitution. These contributions create more complex wave functions of the defect states as presented in Fig. 8(c).

The $C_BC_NV_N$ defect also creates four midgap states that can be associated predominantly with carbon dimer and nitrogen vacancy. However, in this case the structural relaxation leads to a displacement of the C_B atom out of the plane of the monolayer hBN. The lattice reconfiguration modifies the orbital composition of the states that can be visualized by the wave functions of reduced symmetry as presented in Fig. 8(d). The alteration of the orbital states can be seen in the electronic band structure as the emergent spin splitting of all four levels as well as renormalization of the energy of the levels.

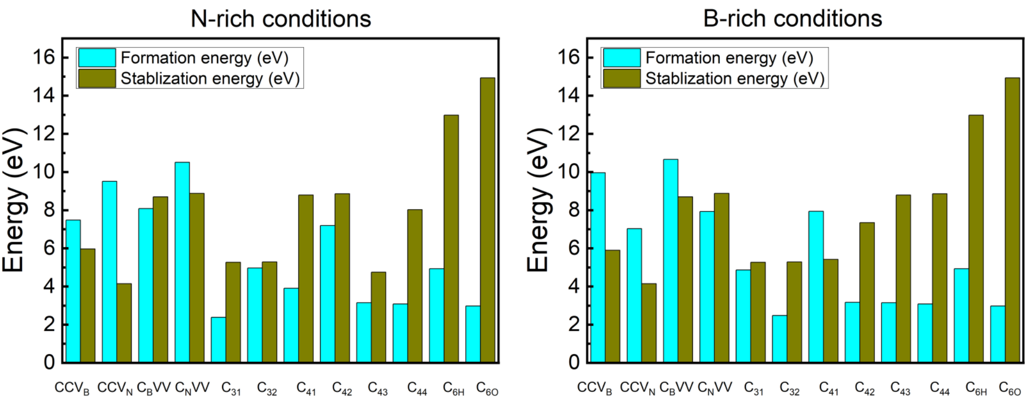

FIG. 7. The histograms present the formation and stabilization energy for triple-site carbon and vacancy centers as well as carbon clusters in hBN in nitrogen-rich and boron-rich conditions.

The donor-acceptor pairing mechanism is also relevant for the formation of carbon clusters, which we investigate based on triple, quadruple, and sextuple carbon substitutions arranged in various configurations within the hBN lattice. The major finding is that every C_NC_B pair within the cluster significantly decreases the formation energy. As a consequence, the quadruple carbon clusters with equal number of C_B and C_N (C_{41} and C_{42}) are characterized by lower formation energy than quadruple carbon clusters with imbalanced number C_B and C_N (C_{43} and C_{44}) and triple carbon substitutions (C_{31}). Among investigated clusters, C6O (an individual carbon hexagonal ring) displays the largest stabilization energy, both in absolute terms and by value normalized per carbon atom. The large stabilization energy of C6O originates from the electron pairing in combination with the delocalized character of the π orbitals within the carbon ring akin to that of

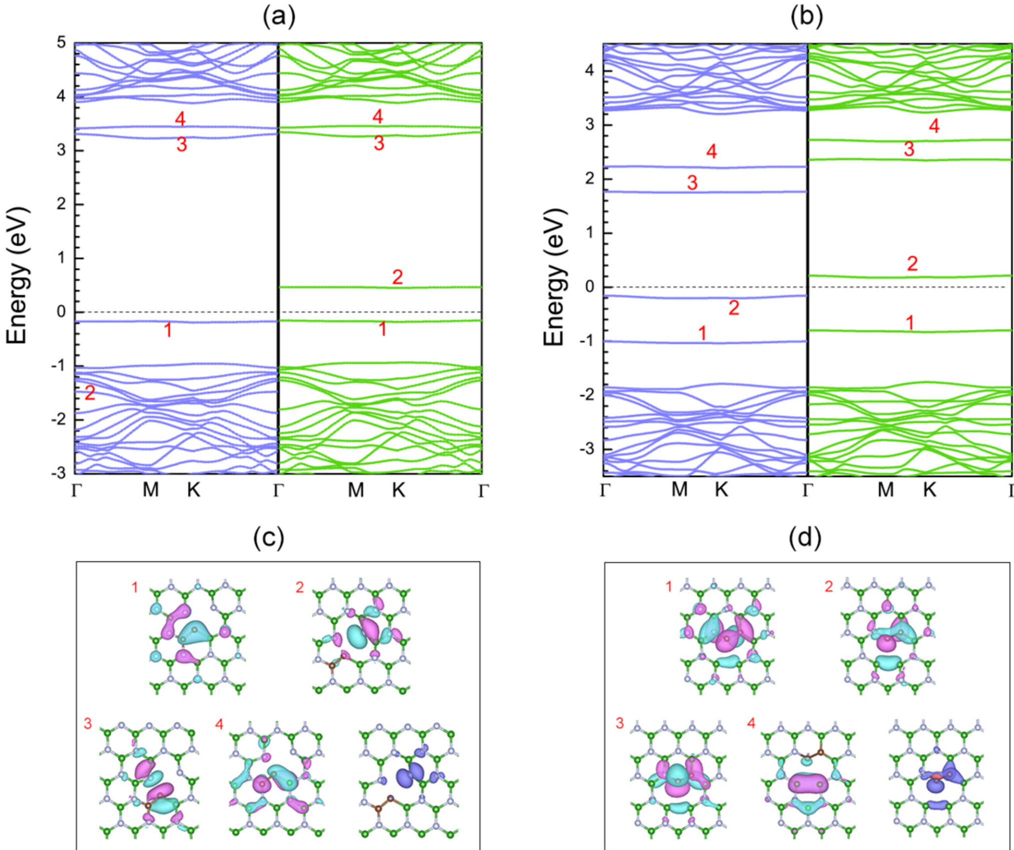

FIG. 8. Spin-projected band structure of hBN in the presence of triple-site centers: (a) $C_BC_NV_B$ and (b) $C_BC_NV_N$. (c),(d) The top view of Γ-point wave functions (real part) illustrate the defect states marked by numbers (1, 2, 3, or 4) in the corresponding band diagrams. The color coding (pink, light blue) represents opposite signs of the wave function. (c),(d) The total spin density is presented with color coding (purple, brown) depicting spin up and down states.

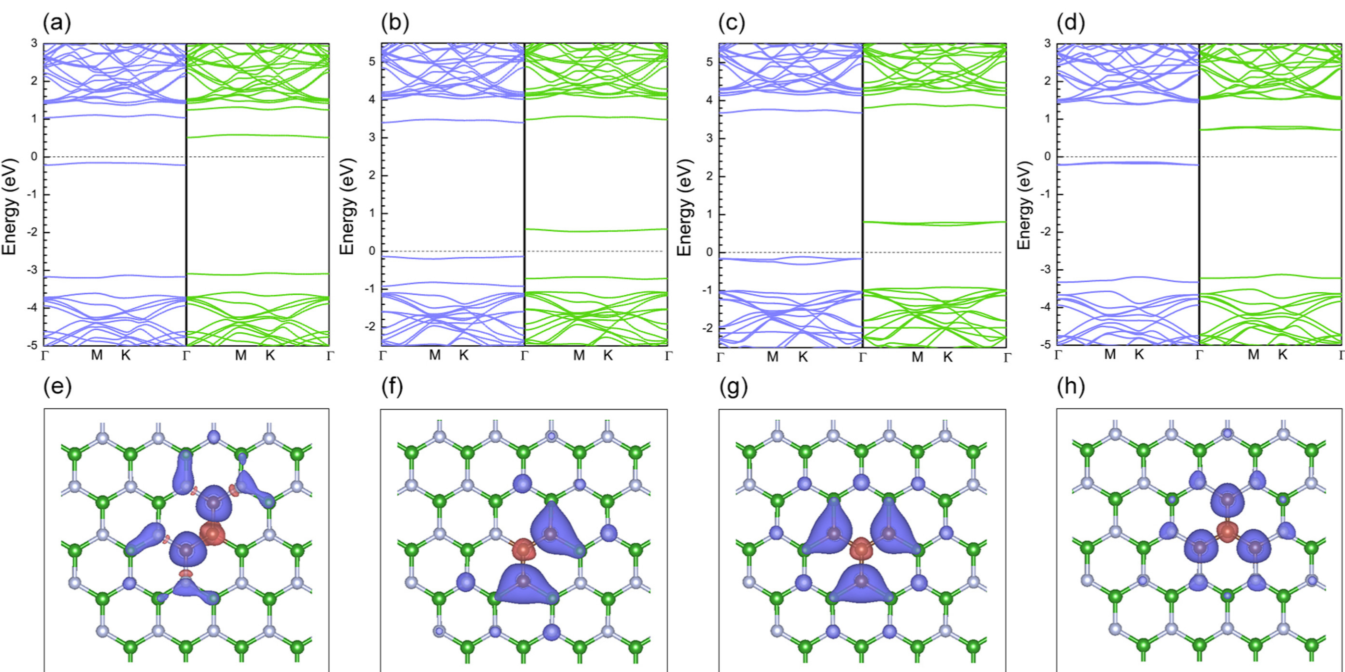

FIG. 9. Spin-projected band structure of hBN in the presence of carbon clusters: (a) C_{31}, (b) C_{32}, (c) C_{41}, and (d) C_{42}. The atomic structure of these clusters is presented in Fig. 2. (e)–(h) The total spin density is presented with color coding (purple, brown) depicting spin up and down states.

a benzene molecule, leading to a significant decrease of the kinetic energy of electrons.

From the point of view of the electronic structure, carbon clusters inherit the states mostly from C-C dimers, C_B and C_N defects as seen in the electronic structure in Figs. 9(a)–9(d) and in the wave functions in Figs. 9(e)–9(h). As in previously discussed cases, carbon dimers introduce empty or fully occupied molecularlike states while excess substitutions give rise to half-filled states above and/or below the conduction band. As a general rule, the total spin associated with the cluster is given by the difference between C_B and C_N lattice sites:

$$S = \frac{|N_{C_N} - N_{C_B}|}{2}.$$

Further examples of the electronic structure for carbon clusters can be found in the Appendix.

IV. CONCLUSIONS

We have investigated the stability and formation mechanisms of defect centers in hBN based on carbon substitution and vacancies within the DFT framework. The band structure of hBN in combination with the electronic configuration of valence electrons of carbon, nitrogen, and boron atoms gives rise to a unique stabilization mechanism through merging of unpaired electrons created by donor and acceptor centers. The proposed mechanism enables a simple understanding of the defect-modified electronic band structure evolving from simple single-site defect towards increasing more complex dimers, trimers, and clusters. Our findings are relevant for the development of novel growth techniques of defect-enriched hBN crystals, postgrowth defect creation methods, and engineering of atomically thin optoelectronic devices operating via defect-induced optical processes.

V. METHODS

A. Crystal growth and sample preparation

Pristine, ultrahigh purity hBN crystals were grown by a high pressure temperature gradient method. The carbon doping was introduced by annealing of pristine crystals in a graphite furnace at 2000 °C for approximately 1 h. The hBN:C films were isolated through mechanical exfoliation of bulk crystals onto Si/SiO_2 substrates. In the transfer process, the substrates were heated to 50 °C to increase the yield of laterally large hBN:C flakes, which exhibit homogeneous and reproducible optical emission. The thickness of the films (typically ranging between few layers to few tens of nanometers) was determined by optical force microscopy.

B. Optical spectroscopy

The PL spectra were measured in backscattering microscopic configuration under 488-nm laser illumination. The sample was cooled down to 1.6 K via a dry system with helium exchange gas acting as the cooling agent for the sample. The Si/SiO_2 substrates with hBN:C were mounted onto piezostages that allow the movement of the sample and positioning the flakes of interest under the microscopy. The PL signal is collected through the same microscopy and collected through a multimode fiber. The emitted light is dispersed by a 0.75-m spectrometer and detected by a charge-coupled device camera.

C. DFT calculations

Our calculations are based on DFT using the PBE functional as implemented in the Vienna *Ab Initio* Simulation Package (VASP) [35–37]. The interaction between the valence electrons and ionic cores is described within the projector augmented wave approach with a plane-wave energy cutoff of 500 eV [38]. Spin polarization was included for all the calculations. The monolayer of hBN and defect calculations were performed using a 50-atom 5×5 supercell, and the Brillouin zone was sampled using a $(12 \times 12 \times 1)$ Monkhorst-Pack grid. The results of the calculations for selected defects were benchmarked against a bigger (10×10) supercell, obtaining within few meV the same formation energy and band structures. A 15-Å vacuum space was used to avoid interaction between neighboring layers. In the structural energy minimization, the atomic coordinates are allowed to relax until the forces on all the atoms are less than 0.01 eV/Å. The energy tolerance is 10^6 eV.

The formation energy, i.e., the energy required to create a defect center, is given by

$$E_f(D) = E(D) - E(\text{hBN}) + \sum_i n_i(\mu_i + E_i),$$

where $E(D)$ is the total energy of the defect center, $E(\text{hBN})$ is the energy of the host hBN, n_i is the number of an element (B, N, or C) transferred from the supercell to the reservoirs, μ_i is the chemical potential defined with respect to the reservoir, i.e., the energy required to move the element from the lattice to the reservoirs, and E_i is the energy of the element in solid/gas phase. Herein, we chose solid boron, N_2 molecule, and graphene to calculate the energy for B, N, and C, respectively. The value of μ_B and μ_N are defined by the growth conditions. There is, however, a constraint on the sum chemical potential: $\mu_B + \mu_N = \mu_{BN}$ where μ_{BN} is the chemical potential of a BN pair established with respect to the reservoirs. This condition entails an upper bound for the chemical potential of N at the N-rich (B-poor) condition, $\mu_N = 0$, where the chemical potential of N is in equilibrium with the reservoir. Similarly, the B-rich (N-poor) condition is defined as $\mu_B = 0$. The calculated formation energy is dependent on the chemical potential of the element especially for nonstoichiometric structures.

The computations of optical properties were carried out through the perturbation theory method implemented in the VASP code. Herein, the imaginary part of the dielectric constant ε_{Im} was computed by summing over the occupied and unoccupied single-particle Kohn-Sham states and the real part of the dielectric constant ε_{Re} was obtained by the Kramers-Kronig transformation. The absorption coefficient was derived from the imaginary and real parts of the dielectric function through the formula

$$I(\omega) = 2\omega\left(\frac{\left[\varepsilon_{\text{Re}}^2(\omega) + \varepsilon_{\text{Im}}^2(\omega)\right] - \varepsilon_{\text{Re}}(\omega)}{2}\right)^{1/2}.$$

ACKNOWLEDGMENTS

This project was supported by the Ministry of Education (Singapore) through the Research Centre of Excellence program (Grant No. EDUN C-33-18-279-V12, I-FIM) and AcRF Tier 3 (MOE2018-T3-1-005). This material is based upon work supported by the Air Force Office of Scientific Research and the Office of Naval Research Global under Award No. FA8655-21-1-7026. K.W. and T.T. acknowledge support from the Elemental Strategy Initiative conducted by the MEXT, Japan (Grant No. JPMXP0112101001) and JSPS KAKENHI (Grants No. JP19H05790 and No. JP20H00354). P.H. acknowledges the National Natural Science Foundation of China (52161037) and support from a scholarship from the Guangxi Education Department (China). The computational work for this paper was performed on resources at the National Supercomputing Centre, Singapore.

[1] R. Schirhagl, K. Chang, M. Loretz, and C. L. Degen, Annu. Rev. Phys. Chem. **65**, 83 (2014).

[2] R.-F. Liu and C. Cheng, Phys. Rev. B **76**, 014405 (2007).

[3] S. Okada, Phys. Rev. B **80**, 161404(R) (2009).

[4] B. Huang and H. Lee, Phys. Rev. B **86**, 245406 (2012).

[5] H. Park, A. Wadehra, J. W. Wilkins, and A. H. C. Neto, Appl. Phys. Lett. **100**, 253115 (2012).

[6] C. Freysoldt, B. Grabowski, T. Hickel, J. Neugebauer, G. Kresse, A. Janotti, and C. G. Van de Walle, Rev. Mod. Phys. **86**, 253 (2014).

[7] L. Weston, D. Wickramaratne, M. Mackoit, A. Alkauskas, and C. G. Van de Walle, Phys. Rev. B **97**, 214104 (2018).

[8] M. Abdi, J.-P. Chou, A. Gali, and M. B. Plenio, ACS Photonics **5**, 1967 (2018).

[9] M. E. Turiansky, A. Alkauskas, and C. G. Van de Walle, Nat. Mater. **19**, 487 (2020).

[10] D. Wang and R. Sundararaman, Phys. Rev. B **101**, 054103 (2020).

[11] Y. Kubota, K. Watanabe, O. Tsuda, and T. Taniguchi, Science **317**, 932 (2007).

[12] G. Cassabois, P. Valvin, and B. Gil, Nat. Photonics **10**, 262 (2016).

[13] T. T. Tran, K. Bray, M. J. Ford, M. Toth, and I. Aharonovich, Nat. Nanotechnol. **11**, 37 (2016).

[14] T. T. Tran, C. Elbadawi, D. Totonjian, C. J. Lobo, G. Grosso, H. Moon, D. R. Englund, M. J. Ford, I. Aharonovich, and M. Toth, ACS Nano **10**, 7331 (2016).

[15] T. T. Tran, C. Zachreson, A. M. Berhane, K. Bray, R. G. Sandstrom, L. H. Li, T. Taniguchi, K. Watanabe, I. Aharonovich, and M. Toth, Phys. Rev. Appl. **5**, 034005 (2016).

[16] M. Koperski, M. R. Molas, A. Arora, K. Nogajewski, A. O. Slobodeniuk, C. Faugeras, and M. Potemski, Nanophotonics **6**, 1289 (2017).

[17] M. Koperski, K. Nogajewski, and M. Potemski, Opt. Commun. **411**, 158 (2018).

[18] M. E. Turiansky, A. Alkauskas, L. C. Bassett, and C. G. Van de Walle, Phys. Rev. Lett. **123**, 127401 (2019).

[19] A. Gottscholl, M. Kianinia, V. Soltamov, S. Orlinskii, G. Mamin, C. Bradac, C. Kasper, K. Krambrock, A. Sperlich, M.

Toth, I. Aharonovich, and V. Dyakonov, Nat. Mater. **19**, 540 (2020).

[20] M. Koperski, K. Pakuła, K. Nogajewski, A. K. Dąbrowska, M. Tokarczyk, T. Pelini, J. Binder, T. Fąs, J. Suffczyński, R. Stępniewski, A. Wysmołek, and M. Potemski, Sci. Rep. **11**, 15506 (2021).

[21] M. Koperski, D. Vaclavkova, K. Watanabe, T. Taniguchi, K. S. Novoselov, and M. Potemski, Proc. Natl. Acad. Sci. USA **117**, 13214 (2020).

[22] Z. Qiu, K. Vaklinova, P. Huang, M. Grzeszczyk, H. Yang, K. Watanabe, T. Taniguchi, K. S. Novoselov, J. Lu, and M. Koperski, arXiv:2110.07842.

[23] M. R. Uddin, J. Li, J. Y. Lin, and H. X. Jiang, Appl. Phys. Lett. **110**, 182107 (2017).

[24] T. Pelini, C. Elias, R. Page, L. Xue, S. Liu, J. Li, J. H. Edgar, A. Dréau, V. Jacques, P. Valvin, B. Gil, and G. Cassabois, Phys. Rev. Materials **3**, 094001 (2019).

[25] M. Mackoit-Sinkevičienė, M. Maciaszek, C. G. Van de Walle, and A. Alkauskas, Appl. Phys. Lett. **115**, 212101 (2019).

[26] A. Sajid and K. S. Thygesen, 2D Mater. **7**, 031007 (2020).

[27] N. Mendelson, D. Chugh, J. R. Reimers, T. S. Cheng, A. Gottscholl, H. Long, C. J. Mellor, A. Zettl, V. Dyakonov, P. H. Beton, S. V. Novikov, C. Jagadish, H. H. Tan, M. J. Ford, M. Toth, C. Bradac, and I. Aharonovich, Nat. Mater. **20**, 321 (2021).

[28] C. Jara, T. Rauch, S. Botti, M. A. L. Marques, A. Norambuena, R. Coto, J. E. Castellanos-Águila, J. R. Maze, and F. Munoz, J. Phys. Chem. A **125**, 1325 (2021).

[29] See Supplemental Material at http://link.aps.org/supplemental/10.1103/PhysRevB.106.014107 for a tabular summary of the formation energy, stabilization energy, magnetic moment, and symmetry of the defect centers considered in this work.

[30] K. Ruedenberg, Rev. Mod. Phys. **34**, 326 (1962).

[31] W. Heitler and F. London, *Quantum Chemistry* (World Scientific, Singapore, 2000), pp. 140–155.

[32] M. Maciaszek, L. Razinkovas, and A. Alkauskas, Phys. Rev. Materials **6**, 014005 (2022).

[33] C. Attaccalite, M. Bockstedte, A. Marini, A. Rubio, and L. Wirtz, Phys. Rev. B **83**, 144115 (2011).

[34] P. Dev, Phys. Rev. Research **2**, 022050(R) (2020).

[35] J. P. Perdew, K. Burke, and M. Ernzerhof, Phys. Rev. Lett. **77**, 3865 (1996).

[36] G. Kresse and J. Furthmüller, Comput. Mater. Sci. **6**, 15 (1996).

[37] G. Kresse and D. Joubert, Phys. Rev. B **59**, 1758 (1999).

[38] P. E. Blöchl, Phys. Rev. B **50**, 17953 (1994).